Optimal Voyage Scheduling of All-electric Ships Considering Underwater Radiated Noise

Roohallah Khatami, Bo Chen, and Yu Christine Chen
Department of Electrical and Computer Engineering
The University of British Columbia
Vancouver, BC, Canada
Email: {roohallah.khatami, cbhp1993, chen}@ece.ubc.ca

Abstract

Underwater radiated noise (URN) emanating from ships can adversely impact the life functions of certain marine mammals that rely on sound to navigate, communicate, and locate prey. This paper formulates an optimal voyage scheduling problem to mitigate the impact of URN on sensitive marine species by choosing amongst different possible paths and specifying the cruising speed along the selected path. We focus on all-electric ships (AESs) owing to their greater flexibility for speed regulation by coordinating an integrated power system. The proposed optimization model schedules generators and energy storage devices toward minimizing the operation cost while satisfying constraints pertinent to URN levels and atmospheric greenhouse gas (GHG) emissions, the electric power network and operational limits, and expected voyage timelines, culminating in a mixed-integer nonlinear programming problem. To promote computational tractability, we approximate the nonlinear relationships for URN, propulsion load, and fuel consumption with piecewise linear functions. This leads to a mixed-integer second-order cone programming problem, which enables convergence to the global optimum and computationally efficient solutions. We illustrate the effectiveness of the proposed model in curbing URN levels and GHG emissions with numerical case studies involving an 18-node ship test system.

Index Terms

All-electric ship, mixed-integer nonlinear programming, optimal voyage scheduling, underwater radiated noise

I. Introduction

Maritime transport is the backbone of worldwide trade and the global economy. During the past few decades, technological advancements in the ship industry have enabled unprecedented expansion in maritime transport with more than 80% of all trade goods currently being carried over the sea, and freight demand is projected to increase by at least three-fold by 2050 [1], [2]. This burgeoning growth has sparked debates regarding the industry's environmental sustainability practices. Indeed, the adequacy of current measures to contain atmospheric greenhouse gases (GHGs) and underwater radiated noise (URN) is questionable, and policymakers are actively working with ship manufacturers and operators to design suitable strategies that help to restrict maritime GHG and acoustic footprints [3], [4]. For example, the International Maritime Organization (IMO) has been compiling a comprehensive

strategy to enforce strict limits on GHG emissions from marine vessels [5], and pertinent amendments recently became enforced [6]. In this regard, all-electric ships (AESs) that employ integrated power systems to supply all shipboard loads are gaining popularity due to their superior operational and energy efficiency [7]. Research pertaining to acoustic footprint of vessels and development of appropriate guidelines and regulations are also ongoing across many jurisdictions around the world (see, e.g., [8]–[12]).

Marine vessels are known to be major sources of URN, a continuous low-frequency noise emanated primarily from ship propulsion systems [13]. Left unchecked, the URN may adversely affect critical life functions of certain marine species, such as killer whales, that rely on sound to navigate, communicate, and locate prey [14]. In order to protect these species, it is imperative to curb URN levels through preventive measures. Indeed, a major recommendation in [8] is to translate the science of URN to guide operational, regulatory, and policy decisions. As an effort in this direction, the European Union project *Achieve QUieter Oceans by shipping noise footprint reduction* (AQUO) aims to design practical guidelines that are concurrently welcomed by shipyards and ship owners [9], [10]. Furthermore, since URN typically increases with cruising speed due to greater propeller cavitation noise [8], the Port of Vancouver in Canada recently orchestrated a voluntary vessel slowdown program called *Enhancing Cetacean Habitat and Observation* (ECHO) to assess the broader implications of lower cruising speed on maritime transport in the Salish Sea [11]. Given the contributing factors to URN, it can potentially be mitigated at the design stage by, e.g., improving the propeller blade design, or during operations by, e.g., suitably coordinating installed equipment [15], [16]. In this paper, we focus on operational strategies to mitigate URN emanating from AESs by selecting alternative paths and regulating cruising speed in a voyage scheduling problem, where we assume that the AES follows a pre-determined timeline and is obliged to be at certain destinations at certain times. Optimal voyage scheduling aims to minimize fuel costs while satisfying the voyage constraints (e.g., on-time arrival at intermediate and destination ports) as well as physical constraints (e.g., supply-demand balance and generator capacity limits).

Past efforts in the literature have addressed the optimal voyage scheduling problem for AESs with emphasis on limiting GHG emissions [17]–[20], eliminating all emissions [21], [22], managing uncertainty in decision making [23], [24], using flexible thermal loads in multi-energy ships [25], [26], and coordinating seaport and ship microgrids [27]. From a broader planning perspective, recent work has focused on coordinated voyage scheduling of a fleet of ships [28], [29]. Central to these papers is recognizing that the propulsion load is directly related to the ship's cruising speed, so regulating the speed effectively renders propulsion motors to be flexible loads that can be optimally scheduled in voyage planning. Moreover, the majority of the aforementioned papers, e.g., [17], [19]–[27], incorporate energy storage (ES) devices that further promote operational flexibility. However, they generally neglect important operational constraints, such as those imposed by the shipboard electric power network and by nodal voltage limits. Furthermore, to the best of our knowledge, no prior work in optimal voyage scheduling has incorporated the impact of URN limitations.

In this paper, we address gaps in the literature and develop a URN-constrained optimal voyage scheduling model for AESs equipped with ES devices. The model culminates in a multi-period optimization problem that minimizes fuel costs while satisfying constraints related to the voyage, URN levels, GHG emissions, and the electrical system. Constraints pertinent to the electric power network are enforced by the so-called *relaxed branch flow model* to avoid

voyage schedules that violate the network limitations. The inclusion of power flow constraints further enables the solved voyage schedule to satisfy limits in nodal voltages and cable current flows toward reliable AES operation. This problem is a mixed-integer nonlinear programming problem, which is in general nonconvex and NP-hard without any global convergence guarantees [30]. To promote solution tractability, we approximate nonlinear functions relating the URN and propulsion power to cruising speed by piecewise linear functions, each of which is associated with a binary auxiliary variable. The linearization technique helps to strike a balance between modelling accuracy and computational complexity, and it enables flexibility to accommodate generic URN models, which are typically characterized via field testing and may differ depending on the ship technology. By including *linearized* URN and voyage constraints along with *nonlinear* power flow equations, the optimal voyage scheduling problem is converted into a mixed-integer second-order cone programming (MISOCP) problem [31]. For each combination of binary variables, the MISOCP reduces to a convex optimization problem with theoretical guarantees for convergence to the global optimum and efficient solution algorithms [31], [32]. In addition to regulating the cruising speed, we embed the flexibility for the AES to choose amongst several possible paths with distinctive URN limits, which can arise due to varying proximity to critical areas inhabited by sensitive marine species. Although optimal path selection aimed at GHG emission mitigation is addressed in [33], the model therein takes discrete values for cruising speed and disregards the limitations imposed by the electric power system and their impact on path selection. In contrast, we model the cruising speed as a continuous variable and explicitly relate the electric power system to the optimal path selection by establishing the propulsion power as a function of cruising speed. In summary, this paper contributes to the state-of-the-art work on optimal voyage scheduling by: i) modelling and constraining the URN emanated from electric ships, ii) enabling the choice of alternative paths between consecutive destinations, iii) embedding constraints imposed by physical limitations of the electric power network, and iv) deploying linearization/relaxation techniques in the solution strategy toward computational tractability. Potential candidates to benefit from our proposed method include ferry routes, such as those offered by BC Ferries, who provide all major passenger and vehicle ferry services for coastal and island communities in the Canadian province of British Columbia [34].

The remainder of the paper is organized as follows. Section II outlines models for the electric power network and loads, as well as operational constraints for voltages, generators, and ES devices. In Section III, we formulate the proposed optimal voyage scheduling problem and apply piecewise linear approximations where appropriate to obtain an MISOCP. Numerical case studies presented in Section IV demonstrate the impact of URN, voltage, and emission constraints on the resulting optimal voyage schedule. Finally, we provide concluding remarks and directions for future work in Section V.

II. Preliminaries

In this section, we introduce models and constraints pertinent to the electric power network, electric loads, generators, and ES devices. To facilitate the model description, we consider a scheduling horizon of the optimal voyage problem from time t_0 to time $t_0 + T$ over, e.g., 12 hours, during which decisions are made at equal intervals of length Δt, e.g., 30 minutes. The endpoints of the decision intervals are collected in the set $\mathcal{T}_{t_0} = \{t_0 + \Delta t, \ldots, t_0 + T\}$.

A. Electric Power Network

Consider the electric power network as a *directed* graph $(\mathcal{N}, \mathcal{E})$, where $\mathcal{N} = \{1, \ldots, N\}$ and $\mathcal{E} = \{(i,j),\ i,j \in \mathcal{N}, j \equiv j(i)\}$ respectively represent the sets of nodes and lines. For node $i \in \mathcal{N}$ at time $t \in \mathcal{T}_{t_0}$, denote its squared voltage magnitude by $w_{i,t}$. Also let $P_i^{\rm load}$ and $Q_i^{\rm load}$ respectively denote the total active- and reactive-power loads connected to node i. Each line $(i,j) \in \mathcal{E}$ is modelled using the lumped-parameter Π-model with series impedance $z_{ij} = z_{ji} = r_{ij} + {\rm j}x_{ij}$ and shunt admittance $y_{ij}^{\rm sh} = y_{ji}^{\rm sh} = g_{ij}^{\rm sh} + {\rm j}b_{ij}^{\rm sh}$. Denote the active- and reactive-power flows in line (i,j) at time $t \in \mathcal{T}_{t_0}$ respectively by $P_{ij,t}^{\rm f}$ and $Q_{ij,t}^{\rm f}$, and the squared magnitude of the line current by $\ell_{ij,t}$. Moreover, denote the set of generators by $\mathcal{G}$, and let $P_{g,t}$ and $Q_{g,t}$ respectively denote the active and reactive power delivered by generator $g \in \mathcal{G}$ at time $t \in \mathcal{T}_{t_0}$. Further collect ES devices in the set $\mathcal{R}$, and suppose that at time $t \in \mathcal{T}_{t_0}$, ES device $r \in \mathcal{R}$ withdraws (delivers) the charging (discharging) power $P_{r,t}^{\rm es,c}$ ($P_{r,t}^{\rm es,d}$), and it delivers reactive power $Q_{r,t}^{\rm es}$. We assume radial configuration for the network topology and accordingly utilize the relaxed branch flow model (see, e.g., [35]). In this model, the active- and reactive-power balance constraints at node $i \in \mathcal{N}$ are given by

$$\begin{aligned}
&\sum_{g\in\mathcal{G}_i} P_{g,t} + \sum_{r\in\mathcal{R}_i} (P_{r,t}^{\rm es,d} - P_{r,t}^{\rm es,c}) - P_{i,t}^{\rm load} \\
&= \sum_{(i,j)\in\mathcal{E}} P_{ij,t}^{\rm f} - \sum_{(k,i)\in\mathcal{E}} (P_{ki,t}^{\rm f} - r_{ki}\ell_{ki,t}) \\
&+ w_{i,t}\bigg(\sum_{(i,j)\in\mathcal{E}} g_{ij}^{\rm sh} + \sum_{(k,i)\in\mathcal{E}} g_{ki}^{\rm sh} \bigg),\ i \in \mathcal{N},\ t \in \mathcal{T}_{t_0}, \qquad (1) \\
&\sum_{g\in\mathcal{G}_i} Q_{g,t} + \sum_{r\in\mathcal{R}_i} Q_{r,t}^{\rm es} - Q_{i,t}^{\rm load} \\
&= \sum_{(i,j)\in\mathcal{E}} Q_{ij,t}^{\rm f} - \sum_{(k,i)\in\mathcal{E}} (Q_{ki,t}^{\rm f} - x_{ki}\ell_{ki,t}) \\
&- w_{i,t}\bigg(\sum_{(i,j)\in\mathcal{E}} b_{ij}^{\rm sh} + \sum_{(k,i)\in\mathcal{E}} b_{ki}^{\rm sh} \bigg),\ i \in \mathcal{N},\ t \in \mathcal{T}_{t_0}, \qquad (2)
\end{aligned}$$

where $\mathcal{G}_i$ and $\mathcal{R}_i$ respectively denote the sets of generators and ES devices connected to node i. The voltage drop between sending end i and receiving end j of a line is calculated as

$$\begin{aligned}
w_{j,t} - w_{i,t} = &-2\left(r_{ij}P_{ij,t}^{\rm f} + x_{ij}Q_{ij,t}^{\rm f}\right) \\
&+ (r_{ij}^2 + x_{ij}^2)\ell_{ij},\ (i,j) \in \mathcal{E},\ t \in \mathcal{T}_{t_0}. \qquad (3)
\end{aligned}$$

Operational limits on squared nodal voltages, line power flows, and squared line currents are imposed by the following:

$$\underline{w}_i \le w_{i,t} \le \overline{w}_i,\ i \in \mathcal{N},\ t \in \mathcal{T}_{t_0}, \qquad (4)$$

$$w_{i,t}\ell_{ij,t} \ge \left(P_{ij,t}^{\rm f}\right)^2 + \left(Q_{ij,t}^{\rm f}\right)^2,\ (i,j) \in \mathcal{E},\ t \in \mathcal{T}_{t_0}, \qquad (5)$$

$$\ell_{ij,t} \le \overline{\ell}_{ij},\ (i,j) \in \mathcal{E},\ t \in \mathcal{T}_{t_0}. \qquad (6)$$

B. Nodal Load Composition

Denote the set of propulsion motors by $\mathcal{M}$. At time $t \in \mathcal{T}_{t_0}$, suppose that the propulsion motor $m \in \mathcal{M}$ consumes active and reactive power $P^{\mathrm{m}}_{m,t}$ and $Q^{\mathrm{m}}_{m,t}$. In (1)–(2), we decompose total active- and reactive-power loads at node $i \in \mathcal{N}$ into service-load components $P^{\mathrm{sr}}_{i,t}$ and $Q^{\mathrm{sr}}_{i,t}$, as well as propulsion-load components $P^{\mathrm{m}}_{m,t}$ and $Q^{\mathrm{m}}_{m,t}$, as follows,

$$P^{\mathrm{load}}_{i,t} = P^{\mathrm{sr}}_{i,t} + \sum_{m \in \mathcal{M}_i} P^{\mathrm{m}}_{m,t},\ i \in \mathcal{N},\ t \in \mathcal{T}_{t_0}, \tag{7}$$

$$Q^{\mathrm{load}}_{i,t} = Q^{\mathrm{sr}}_{i,t} + \sum_{m \in \mathcal{M}_i} Q^{\mathrm{m}}_{m,t},\ i \in \mathcal{N},\ t \in \mathcal{T}_{t_0}, \tag{8}$$

where $\mathcal{M}_i$ denotes the set of propulsion motors connected to node i. Given that the ship cruising speed is a decision variable in the optimal voyage scheduling problem, and the propulsion load is a function of cruising speed, we treat the propulsion motors as flexible loads. The service load includes electrical devices/appliances, e.g., air-conditioner units and electric pumps [26]. In this paper, we neglect potential flexibility in service loads considering that they constitute a much smaller share compared to the propulsion-motor loads. However, we note that flexible service loads can be easily incorporated at the risk of greater burden with respect to notation and size of decision space.

C. Generators

Let the binary variable $I_{g,t} \in \{0, 1\}$ represent the commitment status of generator $g \in \mathcal{G}$ at time $t \in \mathcal{T}_{t_0}$, i.e., $I_{g,t} = 1$ ($I_{g,t} = 0$) indicates that the generator is on (off). Lower and upper limits of generator active- and reactive-power outputs are enforced as follows:[1]

$$\underline{P}_g I_{g,t} \le P_{g,t} \le \overline{P}_g I_{g,t},\ g \in \mathcal{G},\ t \in \mathcal{T}_{t_0}, \tag{9}$$

$$\underline{Q}_g I_{g,t} \le Q_{g,t} \le \overline{Q}_g I_{g,t},\ g \in \mathcal{G},\ t \in \mathcal{T}_{t_0}. \tag{10}$$

Since the voyage scheduling problem may look ahead several hours to days, generators may start up or shut down within the pertinent scheduling horizon. By defining the nonnegative variables $SU_{g,t}$ and $SD_{g,t}$, the startup and shutdown costs of generator g are constrained by

$$SU_{g,t} \ge \mathbb{SU}_g (I_{g,t} - I_{g,t-\Delta t}),\ g \in \mathcal{G},\ t \in \mathcal{T}_{t_0}, \tag{11}$$

$$SD_{g,t} \ge \mathbb{SD}_g (I_{g,t-\Delta t} - I_{g,t}),\ g \in \mathcal{G},\ t \in \mathcal{T}_{t_0}, \tag{12}$$

$$SU_{g,t}, SD_{g,t} \ge 0,\ g \in \mathcal{G},\ t \in \mathcal{T}_{t_0}, \tag{13}$$

where $\mathbb{SU}_g$ and $\mathbb{SD}_g$ are respectively the costs incurred for generator startup and shutdown. Here we assume that the generators are fast enough to neglect their ramping constraints within the decision time interval Δt. In addition, the minimum up and down times of generators are assumed to be less than Δt.

[1]For notational consistency, in this paper, we denote lower and upper limits of variable x by $\underline{x}$ and $\overline{x}$, respectively.

D. Energy Storage Devices

At time $t \in \mathcal{T}_{t_0}$, the energy stored in ES device $r \in \mathcal{R}$ is expressed as follows:

$$E^{\mathrm{es}}_{r,t} = E^{\mathrm{es}}_{r,t-\Delta t} + \Big(\eta^{\mathrm{c}}_r P^{\mathrm{es,c}}_{r,t} - \frac{1}{\eta^{\mathrm{d}}_r} P^{\mathrm{es,d}}_{r,t}\Big)\Delta t, \quad r \in \mathcal{R},\ t \in \mathcal{T}_{t_0}, \tag{14}$$

where η^{c}_r and η^{d}_r respectively represent its charging and discharging efficiency, and where

$$\underline{E}^{\mathrm{es}}_r \le E^{\mathrm{es}}_{r,t} \le \overline{E}^{\mathrm{es}}_r,\ r \in \mathcal{R},\ t \in \mathcal{T}_{t_0}. \tag{15}$$

Further denote the commitment status of ES device $r \in \mathcal{R}$ at time $t \in \mathcal{T}_{t_0}$ in charging and discharging states by the binary variables $I^{\mathrm{es,c}}_{r,t} \in \{0,1\}$ and $I^{\mathrm{es,d}}_{r,t} \in \{0,1\}$, respectively. These binary variables help to establish lower and upper limits imposed on active-power charging and discharging as well as reactive power delivered, as follows:

$$\underline{P}^{\mathrm{es,c}}_r I^{\mathrm{es,c}}_{r,t} \le P^{\mathrm{es,c}}_{r,t} \le \overline{P}^{\mathrm{es,c}}_r I^{\mathrm{es,c}}_{r,t},\ r \in \mathcal{R},\ t \in \mathcal{T}_{t_0}, \tag{16}$$

$$\underline{P}^{\mathrm{es,d}}_r I^{\mathrm{es,d}}_{r,t} \le P^{\mathrm{es,d}}_{r,t} \le \overline{P}^{\mathrm{es,d}}_r I^{\mathrm{es,d}}_{r,t},\ r \in \mathcal{R}, t \in \mathcal{T}_{t_0}, \tag{17}$$

$$\underline{Q}^{\mathrm{es}}_r (I^{\mathrm{es,c}}_{r,t} + I^{\mathrm{es,d}}_{r,t}) \le Q^{\mathrm{es}}_{r,t} \le \overline{Q}^{\mathrm{es}}_r (I^{\mathrm{es,c}}_{r,t} + I^{\mathrm{es,d}}_{r,t}), \quad r \in \mathcal{R},\ t \in \mathcal{T}_{t_0}. \tag{18}$$

Finally, mutual exclusivity of charging and discharging states for ES device r is guaranteed via

$$I^{\mathrm{es,c}}_{r,t} + I^{\mathrm{es,d}}_{r,t} \le 1,\ r \in \mathcal{R},\ t \in \mathcal{T}_{t_0}. \tag{19}$$

Note that although (19) enforces the ES device to either deliver or withdraw active power, (18) enables reactive power delivery in both charging and discharging states. We assume that the ES devices are fast enough to neglect their ramping constraints within the decision time interval Δt.

III. Problem Formulation

The URN emanating from a ship is typically modelled as a function of its cruising speed [11]. Given this, optimizing the cruising speed and generation dispatch by solving a voyage scheduling problem can effectively curb URN levels while minimizing operation cost, satisfying operational limitations, and ensuring punctual arrivals at the designated destinations. Furthermore, the impact of URN on marine mammals can be reduced by scheduling the ship to take alternative paths away from particularly sensitive habitats. In this section, we formulate a URN-constrained voyage scheduling problem that minimizes the AES operation cost subject to the physical constraints imposed by the electric power network, operational limits of generators and ES devices, as well as constraints pertinent to the voyage, the URN, the propulsion load, and the energy efficiency indicator for GHG emissions. Aimed at formulating an MISOCP, we approximate the underlying nonlinear models for operation cost, the URN, and the propulsion loads by mixed-integer linear constraints.

A. The Voyage

Suppose a ship sets off at time t_0 from the origin O and travels to a set of destinations contained in the set $\mathcal{H} = \{1, \ldots, H\}$. In our problem formulation, we manage the URN by regulating cruising speed along a particular path and further reduce the impact of URN on sensitive animals by taking alternative paths farther away from their habitats. To this end, consider a set of Q_h possible paths connecting destination $h-1$ to destination h collected in $\mathcal{Q}_h$. Although there may conceivably be infinitely many paths between destination h and $h-1$, here we assume that other external considerations (e.g., right of way, ocean currents, wind, etc.) result in a finite number of possible paths in $\mathcal{Q}_h$, and small deviations from each path are negligible in the voyage planning problem. Let the binary variable $I^{\mathrm{p}}_{h,q}$ indicate whether the path $q \in \mathcal{Q}_h$ is taken ($I^{\mathrm{p}}_{h,q} = 1$) or not ($I^{\mathrm{p}}_{h,q} = 0$). Considering that only one path between destinations $h-1$ and h should be selected, we impose the following constraint on the path indicator variables:

$$\sum_{q \in \mathcal{Q}_h} I^{\mathrm{p}}_{h,q} = 1, \ h \in \mathcal{H}. \tag{20}$$

Generally speaking, we expect the departure time from each intermediate destination $h \in \mathcal{H}$ and the length of time at berth to be informed by a travel itinerary and pre-specified as inputs to the voyage scheduling problem. Thus, corresponding to the set of intermediate destinations, we accordingly subdivide the entire scheduling horizon $\mathcal{T}_{t_0}$ into H non-overlapping intervals, $\mathcal{T}_{t_0,h}$, $h \in \mathcal{H}$, so that $\bigcup_{h \in \mathcal{H}} \mathcal{T}_{t_0,h} = \mathcal{T}_{t_0}$. Further collect in the set $\mathcal{T}^{\mathrm{b}}_{t_0,h} \subset \mathcal{T}_{t_0,h}$ the time intervals at berth at destination h. Let nonnegative variable $\nu_{h,q,t}$ represent the cruising speed for $t \in \mathcal{T}_{t_0,h}$, $h \in \mathcal{H}$, while travelling along path $q \in \mathcal{Q}_h$. We impose operational limits on the speed with

$$\underline{v} I^{\mathrm{p}}_{h,q} \leq \nu_{h,q,t} \leq \overline{v} I^{\mathrm{p}}_{h,q}, \ h \in \mathcal{H}, \ q \in \mathcal{Q}_h, \ t \in \mathcal{T}_{t_0,h}, \tag{21}$$

so that the speed associated with the chosen path is limited to the range $[\underline{v}, \overline{v}]$ and those associated with all other paths are set to 0. Then let $v_{h,t}$ denote the scheduled speed at time t between destinations $h-1$ and h, which satisfies the following:

$$v_{h,t} = \sum_{q \in \mathcal{Q}_h} \nu_{h,q,t}, \ h \in \mathcal{H}, \ t \in \mathcal{T}_{t_0,h}, \tag{22}$$

$$v_{h,t} = 0, \ h \in \mathcal{H}, \ t \in \mathcal{T}^{\mathrm{b}}_{t_0,h}. \tag{23}$$

In the above, (23) enforces the scheduled speed to be 0 during the pre-specified at-berth time, otherwise (22) sets the scheduled speed to that associated with the chosen path. Finally, let $D_{h,q}$, $q \in \mathcal{Q}_h$, represent the distance spanned by path q between destinations $h-1$ and h. The total distance travelled over $\mathcal{T}_{t_0,h}$ is then constrained by

$$\sum_{t \in \mathcal{T}_{t_0,h}} \nu_{h,q,t} \Delta t = D_{h,q} I^{\mathrm{p}}_{h,q}, \ h \in \mathcal{H}, \ q \in \mathcal{Q}_h. \tag{24}$$

We refer readers to Fig. 1 for a graphical illustration of the voyage scheduling framework with intermediate destinations and alternative paths.

B. Underwater Radiated Noise

Let the URN attributed to path $q \in \mathcal{Q}_h$ at time $t \in \mathcal{T}_{t_0,h}$ be denoted by $U_{h,q,t}$. Typically the URN is modelled as a function of the cruising speed as $U_{h,q,t} = f(\nu_{h,q,t})$, and we assume $f(\cdot)$ is available from the ship manufacturer

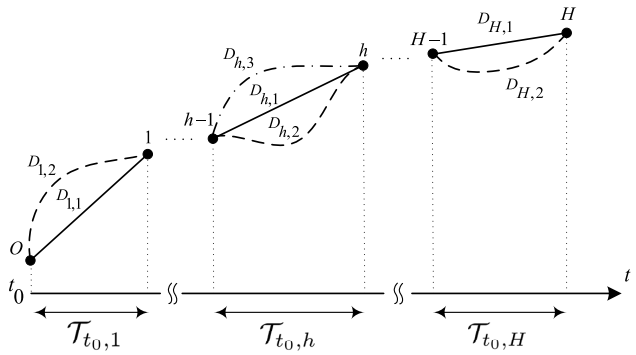

Fig. 1. An illustration of a ship voyage with H destinations. Time steps between consecutive destinations $h-1$ and h are collected in $\mathcal{T}_{t_0,h}$. Multiple paths are possible between consecutive destinations, and each possible path q between destinations $h-1$ and h spans a distance of $D_{h,q}$.

through, e.g., a characteristic curve obtained via field testing [36]. A key advantage to our proposed approach is the ability to deal with any generic URN model, which is accomplished through piecewise linear approximations of the nonlinear function $f(\cdot)$. To this end, suppose $f(\cdot)$ is defined over the range $[\underline{v},\overline{v}]$, and divide this range into S^{u} non-overlapping segments and collect them in the set $\mathcal{S}^{\mathrm{u}}$. Each segment $s\in\mathcal{S}^{\mathrm{u}}$ is confined to endpoints $\widehat{v}_{s-1}$ and $\widehat{v}_s$, so that $[\underline{v},\overline{v}]=\bigcup_{s\in\mathcal{S}^{\mathrm{u}}}[\widehat{v}_{s-1},\widehat{v}_s]$, where $\widehat{v}_0=\underline{v}$ and $\widehat{v}_{S^{\mathrm{u}}}=\overline{v}$. Further define binary and continuous auxiliary variables $I^{\mathrm{u}}_{h,q,s,t}$ and $\varphi_{h,q,s,t}$ for $h\in\mathcal{H},\ q\in\mathcal{Q}_h,\ s\in\mathcal{S}^{\mathrm{u}},\ t\in\mathcal{T}_{t_0,h}$, where $I^{\mathrm{u}}_{h,q,s,t}=1$ ($I^{\mathrm{u}}_{h,q,s,t}=0$) represents the active (inactive) status of the corresponding linearization segment, and each continuous auxiliary variable models the linear function pertinent to the corresponding segment. By calculating the slope of $f(\cdot)$ in each segment $s\in\mathcal{S}^{\mathrm{u}}$ as $\alpha^{\mathrm{u}}_s=\frac{f(\widehat{v}_s)-f(\widehat{v}_{s-1})}{\widehat{v}_s-\widehat{v}_{s-1}}$, we approximate the URN associated with each possible path as the following concatenation of piecewise linear functions:

$$\widehat{U}_{h,q,t}=f(\underline{v})I^{\mathrm{u}}_{h,q,1,t}+\sum_{s\in\mathcal{S}^{\mathrm{u}}}\alpha^{\mathrm{u}}_s\varphi_{h,q,s,t},$$
$$h\in\mathcal{H},\ q\in\mathcal{Q}_h,t\in\mathcal{T}_{t_0,h}. \tag{25}$$

Correspondingly, the cruising speed can be expressed in terms of the auxiliary variables as

$$\nu_{h,q,t}=\underline{v}I^{\mathrm{u}}_{h,q,1,t}+\sum_{s\in\mathcal{S}^{\mathrm{u}}}\varphi_{h,q,s,t},$$
$$h\in\mathcal{H},\ q\in\mathcal{Q}_h,\ t\in\mathcal{T}_{t_0,h}. \tag{26}$$

To guarantee that the linearization segments are deployed sequentially from $s=1$ to $s=S^{\mathrm{u}}$, we impose the following set of constraints:

$$I^{\mathrm{u}}_{h,q,s,t}\le I^{\mathrm{u}}_{h,q,s-1,t},$$
$$h\in\mathcal{H},\ q\in\mathcal{Q}_h,\ s\in\mathcal{S}^{\mathrm{u}}\backslash\{1\},\ t\in\mathcal{T}_{t_0,h}, \tag{27}$$
$$(\widehat{v}_s-\widehat{v}_{s-1})I^{\mathrm{u}}_{h,q,s+1,t}\le\varphi_{h,q,s,t}\le(\widehat{v}_s-\widehat{v}_{s-1})I^{\mathrm{u}}_{h,q,s,t},$$
$$h\in\mathcal{H},\ q\in\mathcal{Q}_h,\ s\in\mathcal{S}^{\mathrm{u}}\backslash\{S^{\mathrm{u}}\},\ t\in\mathcal{T}_{t_0,h}, \tag{28}$$

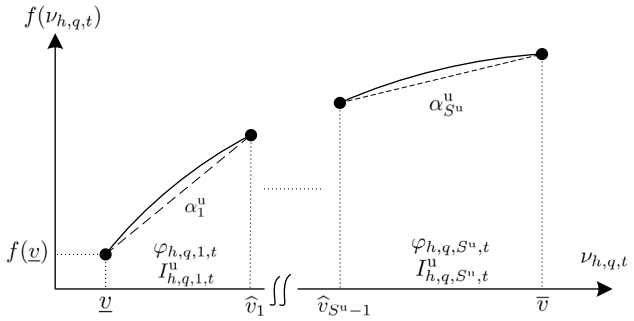

Fig. 2. An illustration of URN linearization dividing the speed range $[\underline{v}, \overline{v}]$ into S^{u} segments. For each segment $s \in \{1, \ldots, S^{\mathrm{u}}\}$, α^{u}_s denotes the slope of the secant connecting the two endpoints of linear approximation, and $I^{\mathrm{u}}_{h,q,s,t}$ and $\varphi^{\mathrm{u}}_{h,q,s,t}$ respectively denote the binary and continuous auxiliary variables modelling the URN-speed segment s at time t for path q connecting destinations $h-1$ and h.

$$0 \leq \varphi_{h,q,s,t} \leq (\widehat{v}_s - \widehat{v}_{s-1}) I^{\mathrm{u}}_{h,q,s,t},$$
$$h \in \mathcal{H},\ q \in \mathcal{Q}_h,\ s = S^{\mathrm{u}},\ t \in \mathcal{T}_{t_0,h}. \tag{29}$$

In the above, (27) ensures that a linearization segment is activated and its pertinent binary variable becomes 1 *only* if all the preceding segments are active, and (28)–(29) guarantee that a linearization segment is fully utilized before activating the next segment. Finally, we limit the URN to the maximum allowable level $\overline{U}_{h,q}$ for the chosen path and set the URN for other paths to exactly zero, as follows:

$$0 \leq \widehat{U}_{h,q,t} \leq \overline{U}_{h,q} I^{\mathrm{p}}_{h,q},\ h \in \mathcal{H},\ q \in \mathcal{Q}_h,\ t \in \mathcal{T}_{t_0,h}. \tag{30}$$

Please refer to Fig. 2 for a graphical illustration of the piecewise linear approximations for the URN-speed relationship.

C. Propulsion Motor Load

For ease of notation, we concatenate the cruising speed values $v_{h,t}$ for all $t \in \mathcal{T}_{t_0,h}$ and $h \in \mathcal{H}$ and further denote the resulting speed simply by v_t, $t \in \mathcal{T}_{t_0}$. The ship propulsion load can then be expressed in terms of cruising speed as

$$P^{\mathrm{pr}}_t = \gamma_1 v_t^{\gamma_2},\ t \in \mathcal{T}_{t_0}, \tag{31}$$

where γ_1 and γ_2 are parameters in the propulsion operating characteristic curve. Similar to the procedure described in Section III-B, we approximate the nonlinear load model with piecewise linear functions. We divide the speed range $[\underline{v}, \overline{v}]$ into S^{m} non-overlapping segments collected in the set $\mathcal{S}^{\mathrm{m}}$. Note that the linearization segments should be determined based on how well they approximate the original nonlinear function, so $\mathcal{S}^{\mathrm{m}}$ need not coincide with $\mathcal{S}^{\mathrm{u}}$. Each segment $s \in \mathcal{S}^{\mathrm{m}}$ is delimited by the endpoints $\widetilde{v}_{s-1}$ and $\widetilde{v}_s$, so that $[\underline{v}, \overline{v}] = \bigcup_{s \in \mathcal{S}^{\mathrm{m}}} [\widetilde{v}_{s-1}, \widetilde{v}_s]$, and $\widetilde{v}_0 = \underline{v},\ \widetilde{v}_{S^{\mathrm{m}}} = \overline{v}$. We further define the binary and continuous auxiliary variables $I^{\mathrm{m}}_{s,t}$ and $\varpi_{s,t}$ for $s \in$

$\mathcal{S}^{\mathrm{m}},\ t \in \mathcal{T}_{t_0}$. Denote the slope of the propulsion load power over each segment $s \in \mathcal{S}^{\mathrm{m}}$ by α_s^{m}, and it is given by $\alpha_s^{\mathrm{m}} = \frac{\gamma_1(\widetilde{v}_s^{\gamma_2} - \widetilde{v}_{s-1}^{\gamma_2})}{\widetilde{v}_s - \widetilde{v}_{s-1}}$. The propulsion power model is then linearized through the following constraints:

$$\widehat{P}_t^{\mathrm{pr}} = \gamma_1 \underline{v}^{\gamma_2} I_{1,t}^{\mathrm{m}} + \sum_{s \in \mathcal{S}^{\mathrm{m}}} \alpha_s^{\mathrm{m}} \varpi_{s,t},\ t \in \mathcal{T}_{t_0}, \tag{32}$$

$$v_t = \underline{v} I_{1,t}^{\mathrm{m}} + \sum_{s \in \mathcal{S}^{\mathrm{m}}} \varpi_{s,t},\ t \in \mathcal{T}_{t_0}, \tag{33}$$

$$I_{s,t}^{\mathrm{m}} \leq I_{s-1,t}^{\mathrm{m}},\ s \in \mathcal{S}^{\mathrm{m}} \backslash \{1\},\ t \in \mathcal{T}_{t_0}, \tag{34}$$

$$(\widetilde{v}_s - \widetilde{v}_{s-1}) I_{s+1,t}^{\mathrm{m}} \leq \varpi_{s,t} \leq (\widetilde{v}_s - \widetilde{v}_{s-1}) I_{s,t}^{\mathrm{m}},$$
$$s \in \mathcal{S}^{\mathrm{m}} \backslash \{S^{\mathrm{m}}\},\ t \in \mathcal{T}_{t_0}, \tag{35}$$

$$0 \leq \varpi_{s,t} \leq (\widetilde{v}_s - \widetilde{v}_{s-1}) I_{s,t}^{\mathrm{m}},\ s = S^{\mathrm{m}},\ t \in \mathcal{T}_{t_0}, \tag{36}$$

where $\widehat{P}_t^{\mathrm{pr}},\ t \in \mathcal{T}_{t_0}$, represents the approximate value of the propulsion load.

At each time t, the total propulsion load is distributed amongst each motor m as

$$P_{m,t}^{\mathrm{m}} = \kappa_m \widehat{P}_t^{\mathrm{pr}},\ m \in \mathcal{M},\ t \in \mathcal{T}_{t_0}, \tag{37}$$

where $0 \leq \kappa_m \leq 1$ is a participation factor that satisfies $\sum_{m \in \mathcal{M}} \kappa_m = 1$. With respect to reactive power, we limit the power factor of propulsion motor $m \in \mathcal{M}$ (possibly equipped with local reactive power compensation) to $\underline{\mathrm{PF}}_m$ as follows:

$$-\tan(\cos^{-1}(\underline{\mathrm{PF}}_m)) P_{m,t}^{\mathrm{m}} \leq Q_{m,t}^{\mathrm{m}} \leq \tan(\cos^{-1}(\underline{\mathrm{PF}}_m)) P_{m,t}^{\mathrm{m}},$$
$$m \in \mathcal{M},\ t \in \mathcal{T}_{t_0}. \tag{38}$$

We also aim to operate each propulsion motor $m \in \mathrm{M}$ near its nameplate power factor $\mathrm{PF}_m^{\mathrm{np}}$ to improve operational efficiency. To this end, we define nonnegative auxiliary variables $Q_{m,t}^{\mathrm{m}+}$ and $Q_{m,t}^{\mathrm{m}-}$, $m \in \mathcal{M}$, $t \in \mathcal{T}_{t_0}$. These respectively represent the positive and negative components of deviations in the propulsion reactive-power consumption from that dictated by the nameplate power factor, which we will later penalize in the optimization problem. For now, the auxiliary variables must satisfy

$$Q_{m,t}^{\mathrm{m}+}, Q_{m,t}^{\mathrm{m}-} \geq 0,\ m \in \mathcal{M},\ t \in \mathcal{T}_{t_0}, \tag{39}$$

$$Q_{m,t}^{\mathrm{m}} - \tan(\cos^{-1}(\mathrm{PF}_m^{\mathrm{np}})) P_{m,t}^{\mathrm{m}} = Q_{m,t}^{\mathrm{m}+} - Q_{m,t}^{\mathrm{m}-},$$
$$m \in \mathcal{M},\ t \in \mathcal{T}_{t_0}. \tag{40}$$

D. Energy Efficiency Operational Indicator

We model the fuel consumption of generator $g \in \mathcal{G}$ by convex function $F_g(P_{g,t})$, which commonly takes quadratic form in practice [37]. In order to linearize the fuel consumption function, divide the power generation range $[\underline{P}_g, \overline{P}_g]$ into S^{e} non-overlapping segments and collect them in the set $\mathcal{S}^{\mathrm{e}}$, where each segment $s \in \mathcal{S}^{\mathrm{e}}$ is confined to the endpoints $\widehat{P}_{g,s-1}$ and $\widehat{P}_{g,s}$, such that $[\underline{P}_g, \overline{P}_g] = \bigcup_{s \in \mathcal{S}^{\mathrm{e}}} [\widehat{P}_{g,s-1}, \widehat{P}_{g,s}]$, $P_{g,0} = \underline{P}_g$, $P_{g,S^{\mathrm{e}}} = \overline{P}_g$. We also define the nonnegative auxiliary variable $p_{g,s,t}$ corresponding to the segment $s \in \mathcal{S}^{\mathrm{e}}$. The slope of fuel consumption function

for segment $s \in \mathcal{S}^{\mathrm{e}}$ is given by $\alpha^{\mathrm{e}}_{g,s} = \frac{F_g(\widehat{P}_{g,s}) - F_g(\widehat{P}_{g,s-1})}{\widehat{P}_{g,s} - \widehat{P}_{g,s-1}}$. Further approximate the nonlinear function $F_g(P_{g,t})$ by the piecewise linear counterpart $\widehat{F}_g(P_{g,t})$, and we develop the following set of linear constraints:

$$\widehat{F}_g(P_{g,t}) = F_g(\underline{P}_g) I_{g,t} + \sum_{s \in \mathcal{S}^{\mathrm{e}}} \alpha^{\mathrm{e}}_{g,s} p_{g,s,t},\ g \in \mathcal{G},\ t \in \mathcal{T}_{t_0}, \tag{41}$$

$$P_{g,t} = \underline{P}_g I_{g,t} + \sum_{s \in \mathcal{S}^{\mathrm{e}}} p_{g,s,t},\ g \in \mathcal{G},\ t \in \mathcal{T}_{t_0}, \tag{42}$$

$$0 \leq p_{g,s,t} \leq \widehat{P}_{g,s} - \widehat{P}_{g,s-1},\ g \in \mathcal{G},\ s \in \mathcal{S}^{\mathrm{e}},\ t \in \mathcal{T}_{t_0}. \tag{43}$$

Note that since $F_g(P_{g,t})$ is convex and the optimal voyage scheduling problem minimizes fuel costs (unlike in the case of the URN and propulsion load models), binary auxiliary variables are not needed.

With the above piecewise linear approximation for the fuel consumption in place, we introduce the energy efficiency operational indicator (EEOI), which is a metric monitored by the ship-owning company through a self-imposed limit. The EEOI represents the mass of CO_2 released per unit of transport work done by the ship [18], [38]. The mass of CO_2 released over the time interval Δt ending at time $t \in \mathcal{T}_{t_0}$ can be obtained as $M^{\mathrm{CO}_2}_t = \lambda_g \widehat{F}_g(P_{g,t}) \Delta t$, where λ_g is the fuel to CO_2-mass conversion factor and $\widehat{F}_g(P_{g,t})$ represents the linearized fuel consumption. Furthermore, the transport work done by the ship over the time interval Δt ending at $t \in \mathcal{T}_{t_0}$ is $W_t = M^{\mathrm{cgo}}_t v_t \Delta t$, where M^{cgo}_t represents the cargo mass for cargo ships or (a scaled factor of) gross tonnage for passenger ships [18], [38]. In general, M^{cgo}_t may vary over the scheduling horizon depending on loading or unloading tasks at the intermediate destinations, e.g., for ferries it is defined as the product of gross tonnage and a positive-valued scaling factor ζ_t [18]. Denote the maximum limit of the EEOI by $\overline{\mathrm{EEOI}}$, and we get the following constraint

$$\sum_{g \in \mathcal{G}} \lambda_g \widehat{F}_g(P_{g,t}) \leq \overline{\mathrm{EEOI}} \cdot M^{\mathrm{cgo}}_t v_t,\ t \in \mathcal{T}_{t_0} \setminus \bigcup_{h \in \mathcal{H}} \mathcal{T}^{\mathrm{b}}_{t_0,h}, \tag{44}$$

where the unit for $\overline{\mathrm{EEOI}}$ depends on the vessel type, e.g., typically $[\mathrm{gCO}_2/\mathrm{tn}{\cdot}\mathrm{nm}]$ for cargo ships and $[\mathrm{gCO}_2/\mathrm{gt}{\cdot}\mathrm{nm}]$ for passenger ships with $[\mathrm{nm}]$ referring to nautical miles and $[\mathrm{gt}]$ to gross tonnage. Furthermore, since the voyage modelling in Section III-A assumes a pre-determined voyage timeline with fixed at-berth time, the emissions incurred while the ship is docked are largely[2] fixed and known beforehand and are thus not subject to optimization. As such, we neglect the at-berth emissions and focus on optimizing cruising emissions. In neglecting the at-berth emissions, we can interpret the maximum emissions limit in (44) as the *net* allowable emissions after discounting by the (largely) fixed at-berth emissions. Before formulating the optimal voyage scheduling problem below, we note that although we use the EEOI as the measure of carbon intensity in this paper, our problem formulation can easily accommodate other similar metrics suitably scaled for a particular voyage. A particular example is the annual efficiency ratio (AER), which is recently regulated by the IMO [6], [39].

[2]It is possible for generators to charge the energy storage devices while at berth, which would lead to variability in the amount of at-berth emissions. However, this amount would be more predictable and considerably less than emissions incurred while cruising.

E. Optimal Voyage Scheduling Problem

Let us denote the fuel price by π_g, $g \in \mathcal{G}$, and a penalty factor regulating the propulsion motor power factors by ρ. The optimal voyage scheduling problem minimizes for the fuel and startup costs of generators, plus the penalty term attributed to reactive power of propulsion motors as

$$\min \sum_{t\in\mathcal{T}_{t_0}} \sum_{g\in\mathcal{G}} \left(\pi_g \widehat{F}_g(P_{g,t})\Delta t + SU_{g,t} + SD_{g,t}\right) + \sum_{t\in\mathcal{T}_{t_0}} \sum_{m\in\mathcal{M}} \rho\left(Q^{\mathrm{m}+}_{m,t} + Q^{\mathrm{m}-}_{m,t}\right) \tag{45a}$$

$$\text{s.t. Electric power network constraints (1)–(6),} \tag{45b}$$

$$\text{Nodal load decomposition (7)–(8),} \tag{45c}$$

$$\text{Generator constraints (9)–(13),} \tag{45d}$$

$$\text{Energy storage constraints (14)–(19),} \tag{45e}$$

$$\text{Voyage and URN constraints (20)–(30),} \tag{45f}$$

$$\text{Propulsion load constraints (32)–(40),} \tag{45g}$$

$$\text{EEOI constraints (41)–(44).} \tag{45h}$$

We emphasize that the problem in (45) is an MISOCP owing to the piecewise linearization technique applied to nonlinear models of the URN, the propulsion load, and the fuel consumption. The MISOCP problem leads to solving convex optimization problems for each combination of binary variables, thus offering theoretical convergence to global optimum and efficient computational performance [31], [32]. On the other hand, without the linearizations, we would need to contend with a mixed-integer nonlinear programming problem, which generally leads to solving a nonconvex NP-hard optimization problem without any global convergence guarantees [30].

Remark. In case the optimal voyage scheduling problem in (45) is infeasible due to URN or EEOI limitations, meaning that the AES cannot abide by the pertinent restrictions, we assume that the ships are either declined the permission to voyage or charged by a preemptively high penalty payment. This arrangement may be internalized in the optimization problem in (45) by introducing slack variables into (30) and (44) and penalizing the associated variables in the cost function (45a). However, given the negligible likelihood of such events in practice, we opt to retain the simpler formulation in (45).

IV. Numerical Results

We perform simulations over a 12-hour scheduling horizon with half-hourly intervals, i.e., $\mathcal{T}_0 = \{0.5, 1, \ldots, 11.5, 12\}$, on the 18-node AC shipboard test system with 4 generators in $\mathcal{G} = \{1, 2, 3, 4\}$ along with 2 ES devices in $\mathcal{R} = \{1, 2\}$ supplying service loads and propulsion motors in $\mathcal{M} = \{1, 2, 3, 4\}$. The one-line diagram for the test system is shown in Fig. 3. Starting from the origin O, the AES travels to 4 destinations contained in $\mathcal{H} = \{1, 2, 3, 4\}$, where two possible paths connect the origin and destination 1 as well as destinations 2 and 3, while only a single path is

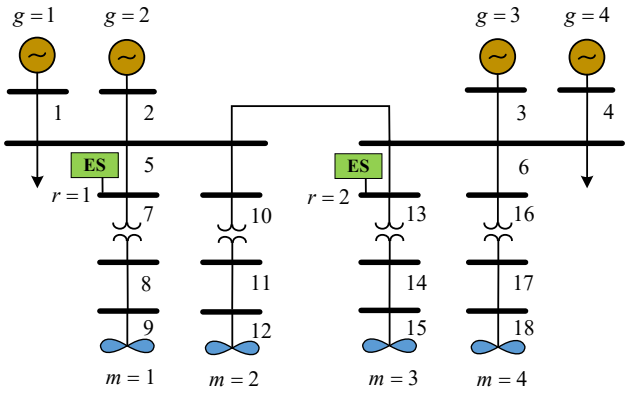

Fig. 3. One-line diagram for an 18-node shipboard test system.

available between destinations 1 and 2 as well as destinations 3 and 4. Unless otherwise stated, parameter values used for numerical case studies presented in this section are reported in Appendix A.

A. Impact of URN and Voltage Constraints

We aim to highlight the impact of URN and voltage constraints on the optimal voyage scheduling of the test shipboard system. To this end, for now we neglect the maximum EEOI constraint (44) and examine the following cases:

- Case 0: URN and voltage limits are neglected,
- Case 1: URN limits are imposed while voltage limits are neglected,
- Case 2: URN and voltage limits are both imposed,

with Case 0 serving as the benchmark. In Case 0, due to the absence of URN limitations, the shortest route of length $D_{1,1} + D_{2,1} + D_{3,1} + D_{4,1} = 153\,[\mathrm{nm}]$ is selected. However, in the constrained Cases 1–2, a longer alternative route of length $D_{1,2} + D_{2,1} + D_{3,2} + D_{4,1} = 157\,[\mathrm{nm}]$ is travelled to avoid violating the URN limits enforced on shorter intermediate paths (i.e., $\overline{U}_{1,1} = \overline{U}_{3,1} = 185\,[\mathrm{dB}]$).

1) Cruising Speed, Propulsion Load, and URN: The optimal ship cruising speed, propulsion power, and URN level for Cases 0–2 are plotted in Fig. 4, where the unit used for the speed is knot $[\mathrm{kn}]$, i.e., nautical miles per hour. For Cases 1–2 and $t \in [0, 1.5] \cup [5, 8.5]\,[\mathrm{hr}]$, the cruising speed increases compared to Case 0 as the ship travels a longer distance within the same required time period (see Fig. 4a). This, in turn, increases the propulsion load accordingly, as shown in Fig. 4b. Although the URN levels increase with higher cruising speeds, as shown in Fig. 4c, they remain below the maximum limit associated with the longer alternative paths (i.e., $\overline{U}_{1,2} = \overline{U}_{3,2} = 190\,[\mathrm{db}]$). At each destination, the ship remains at berth for half hour during which the propulsion power and URN level are both 0. Since the voltage limitations mainly affect reactive-power support, the voyage schedule (largely related to active power) of Case 2 closely follows that of Case 1.

2) Nodal Voltages: We focus on node 9 because it is located at the end of the feeder and is likely to experience the largest voltage drops. The voltage magnitudes at node 9 over time are plotted in Fig. 5. In Case 0, the voltage magnitudes remain within limits as the optimal cruising speed creates a propulsion load that does not engender large

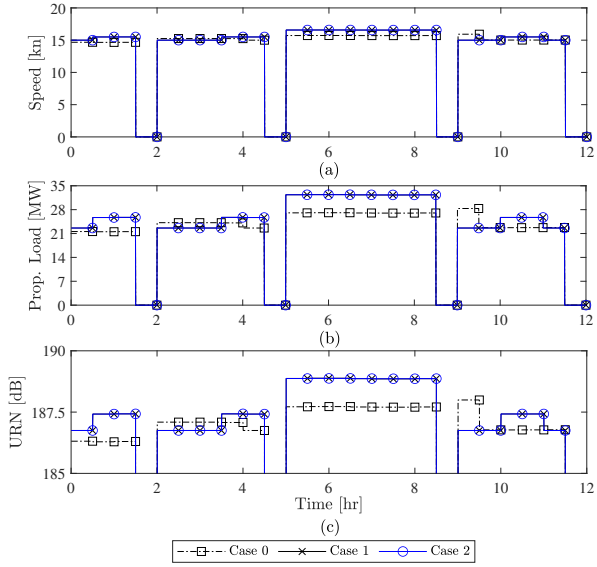

Fig. 4. Optimal values of the ship's (a) cruising speed, (b) propulsion power, and (c) URN level, for Cases 0–2.

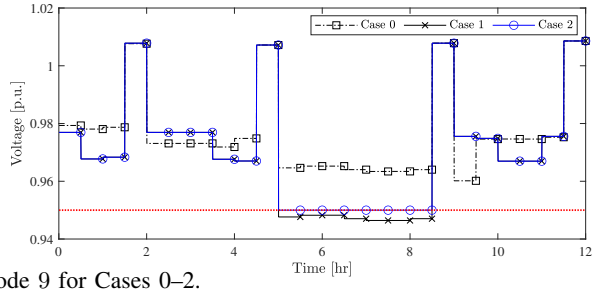

Fig. 5. Voltage magnitudes at node 9 for Cases 0–2.

enough voltage drops within feeders to violate the lower voltage limit (marked by dotted red trace in Fig. 5). In Case 1, increasing the propulsion load causes the lower voltage limit to be violated for $t \in [5, 8.5]$ [hr]. By imposing the voltage constraints in Case 2, however, the voltage violation is avoided by optimally scheduling reactive power, as we discuss next.

3) Generators and ES Devices: The active- and reactive-power schedules of generators and ES devices for Cases 0 and 2 are plotted in Figs. 6 and 7, with the latter also including the stored energy. For ES devices, positive (negative) active-power injection is associated with discharging (charging) states. In Case 0, generators 1, 3, and 4 as well as both ES devices supply the propulsion and service loads for $t \in [0, 1.5] \cup [9.5, 11.5]$ [hr], and for $t \in [2, 4.5] \cup [5, 8.5]$ [hr] all four generators are deployed and ES devices are idle. In addition, for $t \in [1.5, 2] \cup [4.5, 5] \cup [8.5, 9]$ [hr], where the ship is at the intermediate destinations, a subset of generators charge the ES devices and supply the service loads, and for $t \in [11.5, 12]$ [hr], where the ship is at the last destination, only the ES devices supply the service loads. In Case 2, due to the increase in propulsion load, the generator and ES schedules differ substantially from Case 0. The ES devices cease to discharge for $t \in [0, 1.5]$ [hr] and also reduce their discharging power for $t \in [9.5, 11.5]$ [hr] in order to contribute to supplying the increased propulsion load for $t \in [5, 8.5]$ [hr]. Furthermore, generator 2 comes online for $t \in [0, 1.5] \cup [9.5, 11.5]$ [hr] to compensate for the

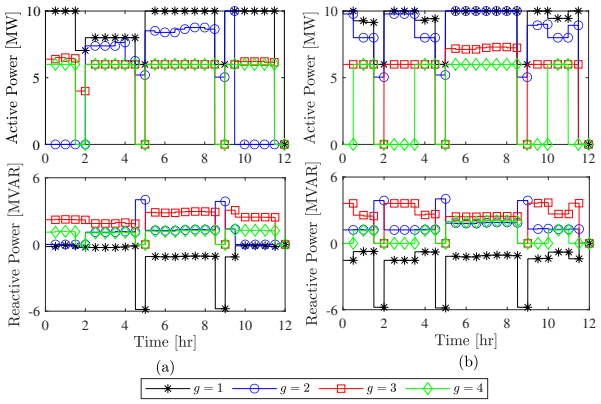

Fig. 6. Optimal active- and reactive-power schedules of generators in (a) Case 0 and (b) Case 2.

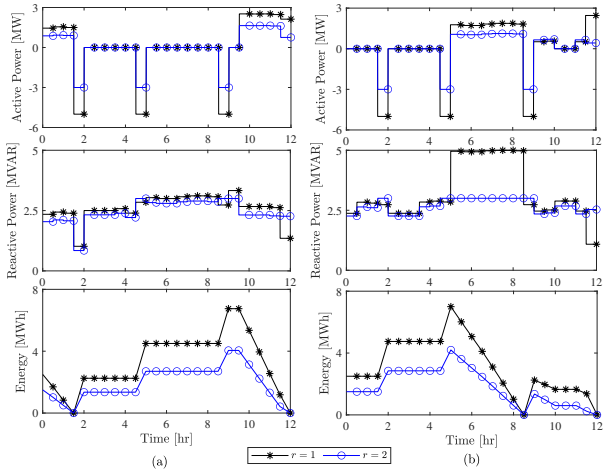

Fig. 7. Active and reactive power and stored energy of ES devices (a) Case 0 and (b) Case 2.

reduction in ES share of supplying load. In Case 2, ES device 1 produces more reactive power (as compared to Case 0) to serve the peak propulsion load for $t \in [5, 8.5]\,[\mathrm{hr}]$. This helps to ensures all voltage magnitudes are within limits. As shown in Fig. 8, the propulsion motor 1 also injects reactive power into the system to help boost the voltage at node 9.

4) Operation Cost: The ship operation cost is \$46,955 in Case 0, \$51,166 in Case 1, and \$51,170 in Case 2. As expected, Case 0 bears the lowest cost while the cost of operation increases for Cases 1 and 2 due to the larger propulsion load. Also, Case 2 incurs a slightly higher cost compared to Case 1 due to the binding minimum voltage limit.

B. Impact of EEOI Constraint

Here we impose the maximum EEOI constraint (44) on Case 2 in Section IV-A. The EEOI values attributed to Case 2 without and with maximum EEOI constraint are plotted in Fig. 9, where the red dotted trace denotes the maximum EEOI limit. The maximum EEOI limit is violated in Case 2 in $t \in [5, 8.5]\,[\mathrm{hr}]$ when the propulsion power increases. By imposing the EEOI constraint, the power output of generator 3 is reduced in $t \in [5, 8.5]\,[\mathrm{hr}]$ and the ES devices discharge at a higher rate to compensate for this reduction (see Fig. 10). As a result, the CO_2

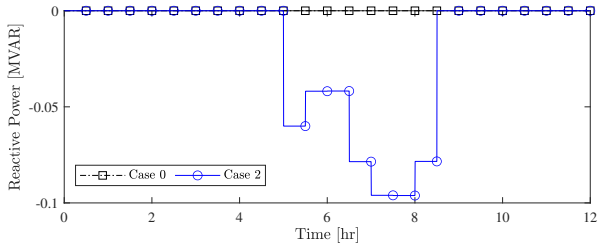

Fig. 8. Reactive power of propulsion motor 1 for Cases 0 and 2.

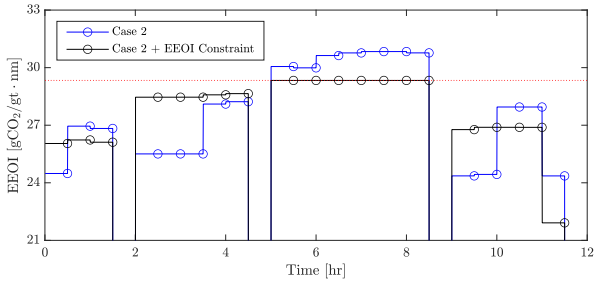

Fig. 9. Energy efficiency operational indicator (EEOI) for (a) Case 2 and (b) Case 2 with EEOI constraint imposed.

emission from generator 3 is reduced and the EEOI is contained within the maximum limit. To enable discharging at a higher rate in $t \in [5, 8.5]$ [hr], the ES devices charge in $t \in [2, 4.5]$ [hr] rather than being idle as in Case 2.

So far in our optimization model and ensuing numerical simulations, we impose the maximum EEOI limit in each time interval, as in (44). Alternatively, our solution approach can easily enforce the EEOI constraint over the entire scheduling horizon as follows:

$$\sum_{t\in\mathcal{T}_{t_0}} \sum_{g\in\mathcal{G}} \lambda_g \widehat{F}_g(P_{g,t}) \leq \overline{\text{EEOI}} \sum_{t\in\mathcal{T}_{t_0}} M_t^{\text{cgo}} v_t. \tag{46}$$

Such an aggregate constraint enables more flexibility in voyage scheduling and is thus less restrictive. On the other hand, for ships operating with a single fuel type (as is the case in the test system shown in 3), the EEOI calculated in (46) is proportional to total fuel cost over the scheduling horizon. Since the fuel cost is the main constituent of the operation cost in (45a), the optimization solution already aligns with minimizing the EEOI. In this way, the aggregate EEOI constraint would not typically be binding, and if it were, the voyage scheduling problem may well be infeasible. On the other hand, for ships that use multiple fuel types, the cost minimization would not necessarily be aligned with minimizing the fuel consumption, and the aggregate EEOI constraint would enable greater flexibility to strike a balance between economic operation and EEOI reduction.

C. Computation Time and Scalability

The proposed optimization problem is modelled in GAMS and solved using the SCIP solver, on a desktop computer with a 3.2 [GHz] i5 processor and 16 [GB] of RAM. Even by choosing a stringent optimality gap of 0.01%, the computation times attributed to different cases do not exceed 30 [min], which is pragmatic for the

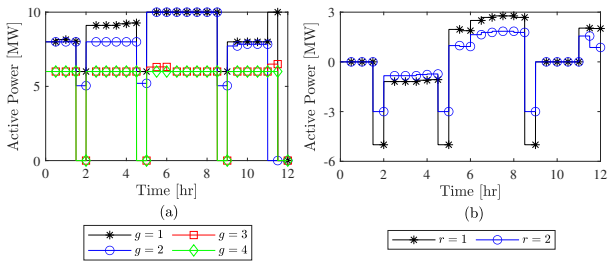

Fig. 10. Active power of (a) generators and (b) ES devices for Case 2 with EEOI constraint imposed.

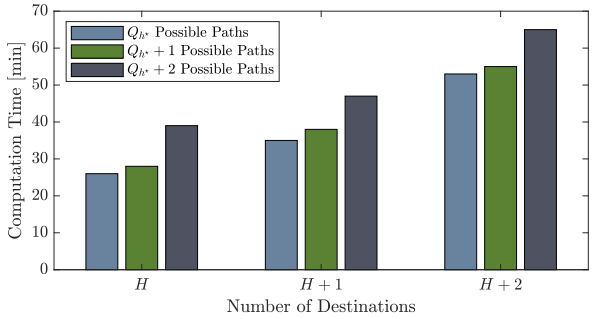

Fig. 11. Computation times for test cases with a total of H, $H + 1$, and $H + 2$ destinations and $Q_{h^\star}$, $Q_{h^\star} + 1$, and $Q_{h^\star} + 2$ possible paths between consecutive destinations $h^\star - 1$ and $h^\star \in \mathcal{H}$.

12-hour ahead voyage scheduling. Note that the 18-node shipboard test system in Fig. 3 is representative of a medium-sized electric ship. Since the size of electric ship power networks is bound by weight, space, and design limitations, we do not expect a considerable increase in the number of generators and nodes even for very large vessels.

To demonstrate the scalability of the proposed voyage scheduling model, we examine the computation times incurred for more destinations and more possible paths between two particular consecutive destinations $h^\star - 1$ and $h^\star \in \mathcal{H}$. Building on Case 2 described in Section IV-A with a total of H destinations and $Q_{h^\star}$ possible paths between consecutive destinations $h^\star - 1$ and $h^\star$, we create new test cases with a total of H, $H + 1$, and $H + 2$ destinations (collected in sets $\{1, \ldots, H\}$, $\{1, \ldots, H, H + 1\}$, and $\{1, \ldots, H, H + 1, H + 2\}$, respectively) and with $Q_{h^\star}$, $Q_{h^\star} + 1$, and $Q_{h^\star} + 2$ possible paths between consecutive destinations (collected in sets $\{1, \ldots, Q_{h^\star}\}$, $\{1, \ldots, Q_{h^\star}, Q_{h^\star} + 1\}$, and $\{1, \ldots, Q_{h^\star}, Q_{h^\star} + 1, Q_{h^\star} + 2\}$, respectively). This results in a total of 9 test cases including the Case 2 of Section IV-A. The optimization solution times plotted in Fig. 11 suggest that: i) the computations times remain practical with additional destinations and possible paths, ii) adding a destination leads to greater increase in the computation time than including an additional possible path between consecutive destinations, and iii) the additional computation time needed increases as total number of destinations and possible paths grow. Potential strategies that can reduce computation times include using more efficient solution algorithms, deploying more powerful computing resources, leveraging parallel computing, and using fewer linearization segments for the nonlinear URN and propulsion motor load models (at the cost of model accuracy).

TABLE I

GENERATOR QUADRATIC FUEL CONSUMPTION COEFFICIENTS AND STARTUP COSTS

Generator g	a_g [MBtu/(MWh)^2]	b_g [MBtu/MWh]	c_g [MBtu]	$\mathbb{SU}_g$ [$]	$\mathbb{SD}_g$ [$]
1	0.54	6.3	39	110	0
2	0.57	6.9	42	110	0
3	1.29	1.2	43.5	50	0
4	1.35	0.99	45	50	0

V. CONCLUSION

In this paper we formulated a comprehensive URN-constrained voyage scheduling problem that minimizes the electric ship operation cost over the voyage scheduling horizon subject to electric power network limitations and the operational limits of generators and ES devices, while respecting the voyage constraints, maximum URN limits, and the energy efficiency indicator limit for GHG emissions. The proposed model enabled evaluating the URN level and containing it within allowable limits by controlling the ship cruising speed and choosing amongst available alternative paths with possibly different URN limits (depending on their proximity to critical areas occupied by sensitive marine species). The numerical studies highlighted the effectiveness of the proposed model in optimally scheduling the generators and ES devices to sustain the desirable speed at which the URN limits are satisfied, and in reliably operating the ship electric power network. Further, we showcased the scalability and computational tractability of the proposed MISOCP problem for greater number of intermediate destinations and alternative paths connecting consecutive destination pairs. Directions for future work include developing voyage scheduling models for convoys of AESs and restricting their URN levels via data-driven geographically-aware methods, assigning different maximum URN limits along each particular path, optimizing voyage timeline in the face of URN restrictions, as well as stochastic modelling extensions to account for uncertainties in environmental factors (e.g., ocean current and wind speed) and the boundaries of critical areas.

APPENDIX

A. Numerical Simulation Parameters

1) Generators: We apply the generator active- and reactive-power limits found in [40]. We further report the coefficients for the quadratic fuel consumption model and generator startup costs in Table I. All generators use the same type of fuel which price is $\pi_g = 10\,[\$/\mathrm{MBtu}]$, $g \in \mathcal{G}$.

2) ES Devices: We list ES parameter values in Table II. The ES devices located at nodes 7 and 13 are initially charged at 2.5 and $1.5\,[\mathrm{MWh}]$, respectively.

3) Electric Power Network: The network topology and pertinent parameter values are sourced from [40]. The voltage of nodes 1 and 3 are fixed at $1.02\,[\mathrm{p.u.}]$. As in [40], we assume that all cables are over-designed and the ship operates well within cable thermal limits.

TABLE II
ENERGY STORAGE DATA

ES r	$\underline{P}_r^{\mathrm{es,c}}/\overline{P}_r^{\mathrm{es,c}}/\underline{P}_r^{\mathrm{es,d}}/\overline{P}_r^{\mathrm{es,d}}$ [MW]	$\underline{Q}_r^{\mathrm{es,c}}/\overline{Q}_r^{\mathrm{es,c}}$ [MVAR]	$\underline{E}_r^{\mathrm{es}}/\overline{E}_r^{\mathrm{es}}$ [MWh]	$\eta_r^{\mathrm{c}}/\eta_r^{\mathrm{d}}$
1	0/5/0/5	−5/5	0/10	0.9/0.9
2	0/3/0/3	−3/3	0/6	0.9/0.9

TABLE III
VOYAGE DATA AND URN LIMITS

Destination h	$T_{t_0,h}$ [hr]	$\mathcal{Q}_h$	$D_{h,q}$ [nm]	$\overline{U}_{h,q}$ [dB]
1	2	$\{1,2\}$	22, 23	185, 190
2	3	$\{1\}$	38	190
3	4	$\{1,2\}$	55, 58	185, 190
4	3	$\{1\}$	38	190

4) The Voyage: Parameters pertinent to the voyage are reported in Table III. We assume that the ship berths at each destination for a single time-interval (half hour).

5) Underwater Radiated Noise: Ross's classical power law model [41] is used to express the URN level in terms of cruising speed as

$$U_{h,q,t} = f(\nu_{h,q,t}) = 10\, c_\nu \log_{10}\left(\frac{\nu_{h,q,t}}{v^{\mathrm{ref}}}\right) + f(v^{\mathrm{ref}}),$$
$$h \in \mathcal{H},\ q \in \mathcal{Q}_h,\ t \in \mathcal{T}_{t_0,h}, \tag{47}$$

where the parameters $c_\nu = 5.08$, $v^{\mathrm{ref}} = 18.88\,[\mathrm{kn}]$, and $f(v^{\mathrm{ref}}) = 192\,[\mathrm{dB}]$ are sourced from [11]. Maximum URN limits along each possible path between consecutive destinations are reported in the rightmost column in Table III.

6) Propulsion and Service Loads: The propulsion load characteristic curve parameters are respectively $\gamma_1 = 0.0067$ and $\gamma_2 = 3$, minimum and nameplate power factors of propulsion motors are respectively $\underline{\mathrm{PF}}_m = 0.9$ and $\mathrm{PF}_m^{\mathrm{np}} = 1$ for $m \in \mathcal{M}$, the penalty factor for power factor regulation is $\rho = 5\,[\$/\mathrm{MVAR}]$, and the ship cruising speed is limited to $[\underline{v}, \overline{v}] = [5, 20]\,[\mathrm{kn}]$ (kn is short for knot). Propulsion power participation factors are set as $[\kappa_m]_{m\in\mathcal{M}} = [0.26, 0.24, 0.26, 0.24]$. In addition, we scale up the service loads connected to nodes 5 and 6 in [40] by the time-dependent scaling factors provided in Fig. 12, in order to highlight the participation of ES devices in supplying the electric loads.

7) Energy Efficiency Operational Indicator: The maximum allowable EEOI is set as $\overline{\mathrm{EEOI}} = 29.3\,[\mathrm{gCO_2/gt{\cdot}nm}]$, the fuel to $\mathrm{CO_2}$-mass conversion factors of generators are set as $\lambda_g = 66\,[\mathrm{kgCO_2/MBtu}]$, $g \in \mathcal{G}$, the gross tonnage of ship is $75{,}000\,[\mathrm{gt}]$, and M_t^{cgo} changes over time according to scaling factor ζ_t given in Fig. 12.

REFERENCES

[1] A. Fratila, I. A. Gavril, S. C. Nita, A. Hrebenciuc *et al.*, "The importance of maritime transport for economic growth in the European Union: A panel data analysis," *Sustainability*, vol. 13, no. 14, pp. 1–23, Jul. 2021.

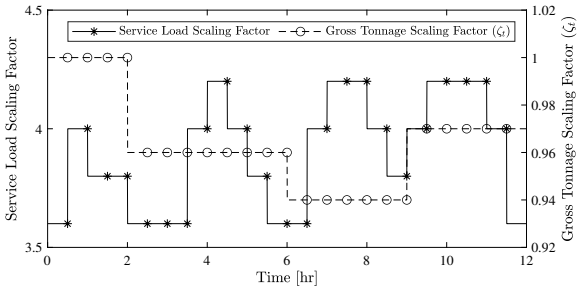

Fig. 12. Service load and gross tonnage scaling factors.

[2] S. E. Hanson and R. J. Nicholls, "Demand for ports to 2050: Climate policy, growing trade and the impacts of sea-level rise," *Earth's Future*, vol. 8, no. 8, p. e2020EF001543, Jul. 2020.

[3] P. Serra and G. Fancello, "Towards the IMO's GHG goals: A critical overview of the perspectives and challenges of the main options for decarbonizing international shipping," *Sustainability*, vol. 12, no. 8, p. 3220, Apr. 2020.

[4] "Long term underwater noise management plan," BC Ferries, 2019. [Online]. Available: https://www.bcferries.com/web_image/hd0/h89/8813696483358.pdf

[5] D. Rutherford and B. Comer, "The international maritime organization's initial greenhouse gas strategy," *International Council on Clean Transportation (ICCT) Policy Updates*, Apr. 2018.

[6] M. E. P. Committee *et al.*, "2021 revised MARPOL Annex VI: Amendments to the annex of the protocol of 1997 to amend the international convention for the prevention of pollution from ships, 1973, as modified by the protocol of 1978 relating there to," *International Maritime Organization, Report*, Jun. 2021.

[7] ——, "Guidelines for the development of a ship energy efficiency management plan (SEEMP)," *International Maritime Organization, Report*, Mar. 2012.

[8] WWF-Canada, "Finding management solutions for underwater noise in Canada's Pacific," Vancouver Aquarium and WWF-Canada, Tech. Rep., Dec. 2013.

[9] C. Audoly, C. Rousset, T. Folegot, M. Andre, L. Benedetti, E. Baudin, and R. Salinas, "AQUO project "achieve quieter oceans by shipping noise footprint reduction."," in *Proc. the 3rd Int. Conf. on Advanced Model Meas. Tech. for the EU Maritime Ind., Gdansk, Poland*, Sep. 2013.

[10] C. Audoly, T. Gaggero, E. Baudin, T. Folegot, E. Rizzuto, R. S. Mullor, M. André, C. Rousset, and P. Kellett, "Mitigation of underwater radiated noise related to shipping and its impact on marine life: A practical approach developed in the scope of AQUO project," *IEEE J. of Oceanic Eng.*, vol. 42, no. 2, pp. 373–387, Apr. 2017.

[11] A. O. MacGillivray, Z. Li, D. E. Hannay, K. B. Trounce, and O. M. Robinson, "Slowing deep-sea commercial vessels reduces underwater radiated noise," *The J. of the Acoust. Soc. of America*, vol. 146, no. 1, pp. 340–351, Jul. 2019.

[12] M. E. P. Committee *et al.*, "Quieting ships to protect the marine environment workshop summary report," *International Maritime Organization, Report*, Mar. 2019.

[13] G. M. Wenz, "Acoustic ambient noise in the ocean: spectra and sources," *The J. of the Acoust. Soc. of America*, vol. 34, no. 12, pp. 1936–1956, Dec. 1962.

[14] W. J. Richardson, C. R. Greene Jr, C. I. Malme, and D. H. Thomson, *Marine mammals and noise*. Academic press, 2013.

[15] C. Audoly, C. Rousset, E. Rizzuto, R. S. Mullor, J. Hallander, and E. Baudin, "Mitigation measures for controlling the ship underwater radiated noise, in the scope of AQUO project," in *Proc. OCEANS 2015-Genova*, May 2015.

[16] A. Kendrick and R. Terweij, "Ship underwater radiated noise," Vard Marine Inc., Tech. Rep. TP 15411 E, Feb. 2019.

[17] F. Kanellos, "Optimal power management with GHG emissions limitation in all-electric ship power systems comprising energy storage systems," *IEEE Trans. on Power Syst.*, vol. 29, no. 1, pp. 330–339, Jan. 2014.

[18] F. D. Kanellos, G. J. Tsekouras, and N. D. Hatziargyriou, "Optimal demand-side management and power generation scheduling in an all-electric ship," *IEEE Trans. on Sust. Energy*, vol. 5, no. 4, pp. 1166–1175, Oct. 2014.

[19] C. Shang, D. Srinivasan, and T. Reindl, "Economic and environmental generation and voyage scheduling of all-electric ships," *IEEE Trans. on Power Syst.*, vol. 31, no. 5, pp. 4087–4096, Sep. 2016.

[20] F. D. Kanellos, A. Anvari-Moghaddam, and J. M. Guerrero, "A cost-effective and emission-aware power management system for ships with integrated full electric propulsion," *Electric Power Systems Research*, vol. 150, pp. 63–75, May 2017.

[21] M. Banaei, M. Rafiei, J. Boudjadar, and M.-H. Khooban, "A comparative analysis of optimal operation scenarios in hybrid emission-free ferry ships," *IEEE Trans. on Transport. Elec.*, vol. 6, no. 1, pp. 318–333, Mar. 2020.

[22] S. Hasanvand, M. Rafiei, M. Gheisarnejad, and M.-H. Khooban, "Reliable power scheduling of an emission-free ship: Multiobjective deep reinforcement learning," *IEEE Trans. on Transport. Elec.*, vol. 6, no. 2, pp. 832–843, Jun. 2020.

[23] S. Fang, Y. Xu, S. Wen, T. Zhao, H. Wang, and L. Liu, "Data-driven robust coordination of generation and demand-side in photovoltaic integrated all-electric ship microgrids," *IEEE Trans. on Power Syst.*, vol. 35, no. 3, pp. 1783–1795, May 2019.

[24] S. Fang and Y. Xu, "Multi-objective robust energy management for all-electric shipboard microgrid under uncertain wind and wave," *International J. of Elec. Power & Energy Syst.*, vol. 117, p. 105600, Oct. 2019.

[25] Z. Li, Y. Xu, S. Fang, X. Zheng, and X. Feng, "Robust coordination of a hybrid ac/dc multi-energy ship microgrid with flexible voyage and thermal loads," *IEEE Trans. on Smart Grid*, Jul. 2020.

[26] Z. Li, Y. Xu, S. Fang, Y. Wang, and X. Zheng, "Multiobjective coordinated energy dispatch and voyage scheduling for a multienergy ship microgrid," *IEEE Trans. on Industry Appl.*, vol. 56, no. 2, pp. 989–999, Apr. 2020.

[27] S. Fang, Y. Wang, B. Gou, and Y. Xu, "Toward future green maritime transportation: An overview of seaport microgrids and all-electric ships," *IEEE Trans. on Vehicular Tech.*, vol. 69, no. 1, pp. 207–219, Jan. 2020.

[28] Y. Kisialiou, I. Gribkovskaia, and G. Laporte, "Robust supply vessel routing and scheduling," *Transportation Research Part C: Emerging Technologies*, vol. 90, pp. 366–378, 2018.

[29] ——, "Supply vessel routing and scheduling under uncertain demand," *Transportation Research Part C: Emerging Technologies*, vol. 104, pp. 305–316, 2019.

[30] P. Belotti, C. Kirches, S. Leyffer, J. Linderoth, J. Luedtke, and A. Mahajan, "Mixed-integer nonlinear optimization," *Acta Numerica*, vol. 22, pp. 1–131, Apr. 2013.

[31] H. Y. Benson and Ü. Sağlam, "Mixed-integer second-order cone programming: A survey," in *Theory Driven by Influential Applications*. INFORMS, Oct. 2014, pp. 13–36.

[32] Z. Cai and K.-C. Toh, "Solving second order cone programming via a reduced augmented system approach," *SIAM J. on Optimization*, vol. 17, no. 3, pp. 711–737, Sep. 2006.

[33] L. Zhen, Z. Hu, R. Yan, D. Zhuge, and S. Wang, "Route and speed optimization for liner ships under emission control policies," *Transportation Research Part C: Emerging Technologies*, vol. 110, pp. 330–345, 2020.

[34] BC Ferries. [Online]. Available: https://www.bcferries.com/

[35] M. Farivar and S. H. Low, "Branch flow model: Relaxations and convexification—part I," *IEEE Trans. on Power Syst.*, vol. 28, no. 3, pp. 2554–2564, Aug. 2013.

[36] M. A. Bahtiarian, "ASA standard goes underwater," *Acoust. Today*, vol. 5, no. 4, pp. 26–29, Oct. 2009.

[37] A. J. Wood, B. F. Wollenberg, and G. B. Sheblé, *Power generation, operation, and control*. John Wiley & Sons, 2013.

[38] M. E. P. Committee *et al.*, "Guidelines for voluntary use of the ship energy efficiency operational indicator (EEOI)," *International Maritime Organization, Report*, Aug. 2009.

[39] W. S. Sou, T. Goh, X. N. Lee, S. H. Ng, and K.-H. Chai, "Reducing the carbon intensity of international shipping–the impact of energy efficiency measures," *Energy Policy*, vol. 170, p. 113239, 2022.

[40] T. L. Baldwin and S. A. Lewis, "Distribution load flow methods for shipboard power systems," *IEEE Trans. Ind. Appl.*, vol. 40, no. 5, pp. 1183–1190, Sep./Oct. 2004.

[41] D. Ross and W. Kuperman, "Mechanics of underwater noise," Oct. 1989.